

White Light Generation From YAG:Ce-Doped Phosphate Glass-Based Composite Fibers

Khaldoon Nasser,* Hùng Nguyễn Trân, Arjun Vakkada Ramachandran, Mikko Närhi, Turkkka Salminen, Catherine Boussard-Plédel, Johann Troles, Tian-Long Guo, Matthieu Roussey, and Laeticia Petit

The growing demand for next-generation lighting technology is driving efforts to develop white light-emitting fibers for potential applications in medical endoscopy, sensing, telecommunication, and integrated photonics. In this work, a new white light-emitting composite fiber based on YAG:Ce³⁺ phosphors embedded in a phosphate glass is developed. The glass matrix composition is precisely tailored to enhance the thermal stability of the glass to allow fiber drawing while matching the refractive index with the phosphors to ensure the transparency of the composite. Comprehensive analyses of the spectroscopic and structural properties reveal significant interfacial reactions between the glass and YAG:Ce³⁺ phosphor particles during composite preparation, including phase changes, elemental diffusion, and partial decomposition. Despite these effects, the YAG:Ce³⁺ phosphors retain their white light emission properties throughout both preform melting and fiber drawing. Light propagation in the fiber, despite the presence of the phosphors in the fiber, as well as white light emission upon blue excitation are demonstrated.

1. Introduction

The development of next-generation lighting technologies has increasingly focused on the generation and delivery of white light via optical fibers. White light-emitting fibers (WLEFs) form a transformative solution for a broad range of applications, including medical endoscopy, artificial lighting, remote sensing, light fidelity (LiFi), and communication technologies.^[1–5] Unlike conventional broadband sources, WLEFs offer the unique advantage of flexible and localized light delivery while maintaining the high brightness and spectral continuity. The growing demand for compact, robust, and high-efficiency white light sources that can reach over long distances has stimulated intensive research on novel material systems and fabrication methodologies.^[6,7]

Rare-earth (RE) doped fibers have become a primary option for broadband light sources. They are known for their high brightness and good beam quality, making them suitable for applications like sensing, optical coherence tomography (OCT), imaging, and fiber optic gyroscopes.^[8,9] Despite their advantages, RE-doped fibers typically exhibit emission bandwidths below 100 nm, primarily obtained using energy transfer between donors (Nd³⁺, Yb³⁺) and acceptors (Eu³⁺, Tm³⁺, Er³⁺).^[8–11] The use of energy transfer to obtain broadband emission in optical fibers raises the issue of optimizing the concentration and ratio of RE donors and acceptors.^[11] The glass matrix should allow fiber drawing and also should have low phonon energy to avoid concentration quenching, which negatively affects energy transfer efficiency.^[12,13] For applications requiring broader spectral coverage, researchers have been exploring various approaches, including supercontinuum fiber lasers. Supercontinuum sources offer exceptionally broad spectral coverage, from 400 to 1700 nm, making them ideally suitable for spectroscopy, imaging, and metrology.^[5,14] However, the cost of supercontinuum laser systems remains a major barrier; even low-power models often exceed thousands of dollars, limiting their practicality and applications.

Another approach for realizing WLEFs involves embedding quantum dots (QDs) or nanoparticles within fiber structures, offering promising potential for flexible white light emission.

K. Nasser, H. N. Trân, A. V. Ramachandran, M. Närhi, L. Petit
Photonics Laboratory
Tampere University
Korkeakoulunkatu 3, Tampere 33720, Finland
E-mail: khaldoon.nasser@tuni.fi

T. Salminen
Tampere Microscopy Center
Tampere University
Tampere 33014, Finland

C. Boussard-Plédel, J. Troles
Univ Rennes
CNRS
ISCR [(Institut des Sciences Chimiques de Rennes)] – UMR 6226
Rennes F-35000, France

T.-L. Guo, M. Roussey
Center for Photonics Sciences
University of Eastern Finland
P.O. Box 111, Joensuu FI-80101, Finland

 The ORCID identification number(s) for the author(s) of this article can be found under <https://doi.org/10.1002/adom.202503741>

© 2026 The Author(s). Advanced Optical Materials published by Wiley-VCH GmbH. This is an open access article under the terms of the [Creative Commons Attribution License](#), which permits use, distribution and reproduction in any medium, provided the original work is properly cited.

DOI: 10.1002/adom.202503741

Recent studies have demonstrated the successful integration of CdSe/CdS colloidal QDs into polymer optical fibers, achieving stable luminescence and high photoluminescence quantum yields.^[15,16] These composite polymer fibers, fabricated via thermal drawing or electrospinning techniques, maintain mechanical flexibility and exhibit uniform light emission along the fiber length. However, they have significant drawbacks; poor stability leading to degradation of the temperature-sensitive QDs under the high processing temperatures, poor dispersion, and QD agglomeration, causing uneven luminescence. Additionally, the moisture sensitivity of the QDs in the polymer fiber can further reduce the long-term stability.^[17,18]

One of the most promising approaches to generate high-quality white light involves the use of cerium-doped yttrium aluminum garnet (YAG:Ce³⁺) phosphors.^[19–21] YAG:Ce³⁺ is an inorganic, ceramic-based down-conversion phosphor, which is easy to synthesize, integrate, mass-produce, and is available commercially.^[21,22] YAG:Ce³⁺ efficiently converts blue or UV excitation into broad-spectrum green-red emission, and when combined with a blue light-emitting diode (LED) or laser diode, bright white light can be produced.^[20,23] YAG:Ce³⁺ shows excellent luminous performance with high quantum efficiency ($\approx 90\%$).^[24] YAG:Ce³⁺ phosphors are thermally and chemically stable, non-toxic, and maintain brightness and spectral properties under high-power excitation from LED.^[23]

Various forms of YAG:Ce³⁺-based light sources have been explored, including bulk crystals,^[25] ceramics,^[21,22] and films.^[26] However, each configuration has inherent drawbacks that limit its integration into fiber systems. Bulk crystals and ceramics are difficult to shape and integrate into fiber architecture, whereas film structures face challenges, including poor moisture resistance and thermal degradation, just to name a few.^[21,25,26] Organic resin adhesives or silicon are usually used to encapsulate YAG:Ce³⁺ phosphors or films. However, these materials have poor heat resistance. Under the high-power excitation from the LEDs, the internal organic matter becomes yellow or black due to heat accumulation, resulting in a degradation in transparency and luminance.^[27,28]

To overcome these limitations, researchers have been focusing on using sintering methods to embed YAG:Ce³⁺ phosphors in different glass systems, such as tellurite,^[23,29] silicate,^[30] and phosphates.^[31,32] The phosphor-in-glass approach offers significant advantages over the traditional resin-encapsulated phosphor, including enhanced chemical and thermal stability and uniform phosphor distribution, which leads to improved luminous efficacy, better heat dissipation, and greater long-term reliability for high-power lighting applications.^[29–32] Phosphate glasses are considered promising candidates to host YAG:Ce³⁺ phosphor. They have relatively low melting temperatures, which minimizes the risk of thermal degradation of embedded phosphors, thereby preserving luminescent performance during both composite fabrication and fiber drawing.^[24,31,32] Additionally, phosphate glasses show excellent luminous performance with high quantum efficiency under blue excitation when doped with YAG:Ce³⁺.^[24,31] However, the most fundamental issue in the sintering method is how to preserve the intactness of the embedded phosphors during the heat treatment and calcination so that the composites could retain the luminescence properties of the raw phosphors and allow for further fabrication processes like fiber drawing. Be-

sides, this method demands complex processes as well as special, costly equipment.

Many studies have focused on the addition of pre-synthesized crystals to the molten glass before quenching.^[33–35] This method allows for control over the spectroscopic properties of the incorporated crystals independently of the glass composition. An ideal host should possess a refractive index closely matching that of the phosphors, thereby enhancing transparency and minimizing scattering.^[36,37] Additionally, the phosphors must be uniformly dispersed throughout the glass matrix without aggregation to ensure consistent optical performance.^[38] To enable further processing, such as fiber drawing, the glass should maintain high thermal stability after adding the crystals. Zhao et al drew low-loss fiber from a transparent tellurite glass doped with upconversion nanocrystals.^[35] Lemiere et al prepared preforms by remelting a glass with SrAl₂O₄·Eu²⁺, Dy³⁺ phosphors,^[39] and these preforms were then drawn into fibers, resulting in composite fibers exhibiting green afterglow after UV charging. Lee et al drew tellurite fiber doped with Er-doped YAlO₃ microcrystals from a preform prepared using volumetric interface doping.^[40] Recently, Vakula et al prepared a composite fiber from phosphate glass preform containing LiNbO₃:Yb³⁺ crystals.^[34]

To the best of our knowledge, there have been no reports on composite fibers made of glass with embedded YAG:Ce³⁺. The challenge lies in the combination of thermal stability, mechanical robustness, and optical properties. In this work, we successfully fabricate an optical fiber from a YAG:Ce³⁺ containing composite. First, we precisely tailor the phosphate glass composition to obtain a thermally stable glass with a refractive index similar to that of the phosphor. Second, we add the YAG:Ce³⁺ phosphors to the glass and investigate the structural and spectroscopic properties of the resulting composite to understand the interaction between the phosphor and the glass host. Finally, we draw the composite fiber and demonstrate successful light propagation in the fiber despite the presence of the phosphors in the fiber as well as white light emission upon blue excitation.

2. Results and Discussion

Selecting the right glass matrix for YAG:Ce³⁺ phosphors is crucial for achieving desired optical properties. The key considerations include the glass's refractive index and thermal stability. Matching the refractive indices of the glass matrix and the phosphors is essential to obtain a transparent composite and reduce the scattering,^[36,37] whereas the good thermal stability against crystallization enables fiber fabrication.^[41] The phosphate glass system 75NaPO₃-25CaO (in mol%) is known for its good thermal stability with $\Delta T > 100^\circ\text{C}$.^[42] However, its refractive index (≈ 1.5) is much lower than that of YAG phosphor (1.83).^[43] Increasing the refractive index of a glass can be achieved by adding high-polarizability oxides such as Nb₂O₅.^[44–46] Therefore, phosphate glasses with the composition of (75-x/2)NaPO₃ - (25-x/2)CaO - xNb₂O₅ (in mol%), where x = 10, 20, 25 mol% (referred to as Nb10, N20 and Nb25, respectively), were prepared by the melt-quenching process to produce glass with a refractive index closely matching that of YAG:Ce³⁺. The amorphous nature of the glasses was confirmed from their XRD patterns that show broad humps without any sharp peaks (Figure S1a, Supporting Information). As expected, increasing the concentration of Nb₂O₅ leads to

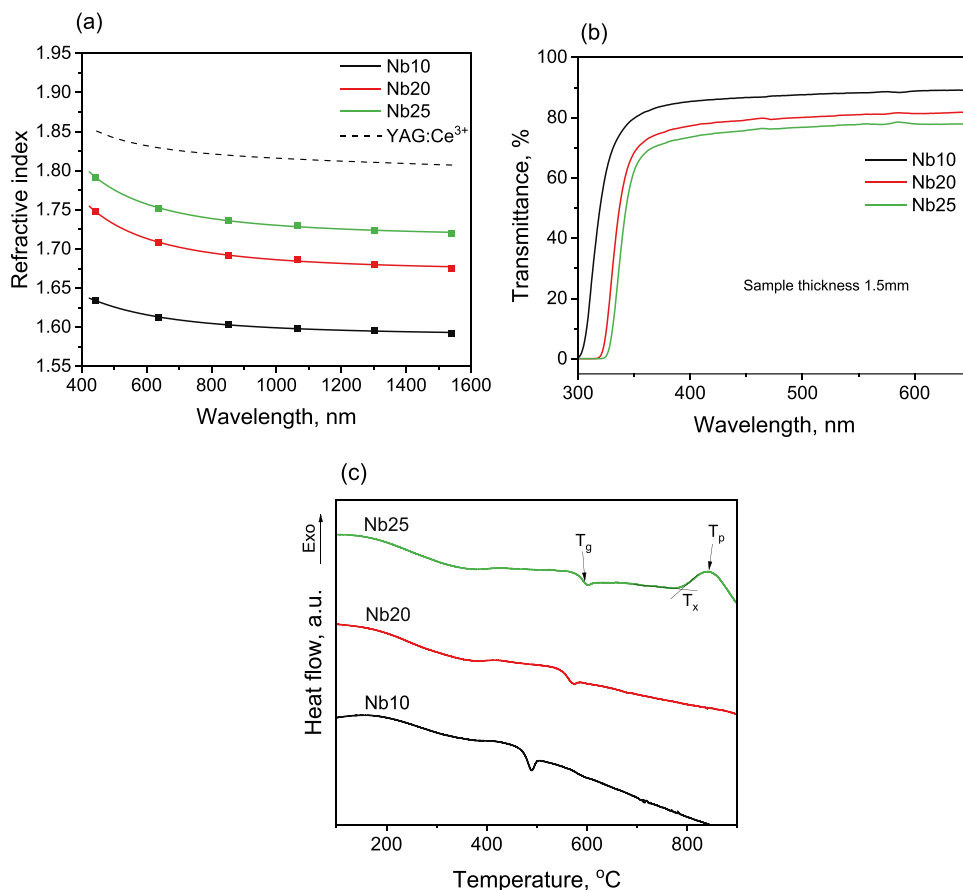


Figure 1. a) Refractive index dispersion of the glasses and the YAG:Ce³⁺. b) Transmittance spectra of the glasses in the 300–650 nm region. c) Thermogram of the glasses.

significant rises in the refractive index, thereby reducing the mismatch in the refractive indices between the glass matrix and YAG:Ce³⁺, as shown in **Figure 1a**.

Increasing the Nb₂O₅ content shifts the UV absorption edge toward longer wavelengths (Figure 1b). The redshift of the UV absorption edge is evidenced from the yellow coloration of the glasses when increasing the Nb₂O₅ content (inset of Figure S1a, Supporting Information). The incorporation of Nb₂O₅ into the glass network does have an impact on the thermal properties of the glass (Figure 1c and Table 1). Increasing the concentration of Nb₂O₅ in the glass composition leads to a rise in T_g . No crystallization signals are observed in the Nb10 and Nb20, whereas the thermogram of Nb25 shows an exothermic peak, indicating that this glass is more prone to crystallization compared to the

others. Nonetheless, Nb25 is expected to still possess good thermal stability against crystallization as evidenced by its large ΔT ($T_x - T_g$) = 194 °C. All glasses are thus excellent candidates for fiber drawing.^[41] As the Nb₂O₅ concentration increases, the density of the glass increases (Table 1), which is expected due to the higher molecular weight of Nb₂O₅ (265.81 g mol⁻¹) compared to that of NaPO₃ (101.96 g mol⁻¹) and CaO (56.08 g mol⁻¹). As expected, the molar volume (V_m) of the glass increases as well when increasing the Nb₂O₅ concentration. This is due to the large amount of oxygen atoms that have a high ionic radius (O²⁻: 1.40 Å) compared to the other ions (Na⁺: 0.99 Å, P⁵⁺: 0.17 Å, Ca²⁺: 1 Å, Nb⁵⁺: 0.64 Å).^[47]

The structural changes induced by the addition of Nb₂O₅ are evident from the Raman and FTIR spectra of the glasses, shown

Table 1. Physical and thermal characteristics of the glasses. ρ is the glass density, V_m is the glass molecular weight, T_g is the glass transition temperature, T_x is the onset crystallization temperature, T_p is the peak crystallization temperature, and ΔT is defined as $T_x - T_g$.

Glass	ρ [g cm ⁻³] ± 0.02 g cm ⁻³	V_m [cm ³ mol ⁻¹] ± 0.05 cm ³ mol ⁻¹	T_g [°C] ± 3 °C	T_x [°C] ± 3 °C	T_p [°C] ± 3 °C	$\Delta T = T_x - T_g$ [°C] ± 6 °C
Nb10	2.96	36.88	484	–	–	–
Nb20	3.21	39.83	561	–	–	–
Nb25	3.32	41.32	592	786	842	194

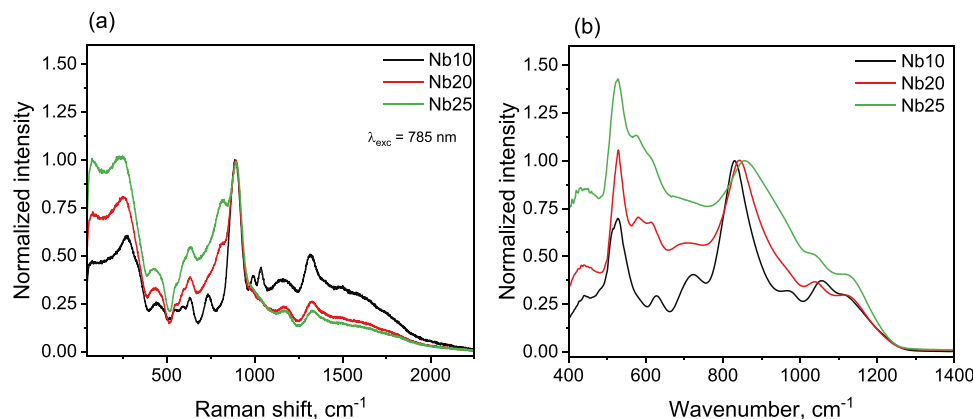


Figure 2. a) Raman spectra of the glasses ($\lambda_{\text{exc}} = 785 \text{ nm}$). b) ATR-FTIR spectra of the glasses.

in **Figure 2a,b**, respectively. The Raman spectra show broad bands centered around 250, 425, 630, 820, 890, 1170, and 1315 cm^{-1} . The band at 1315 cm^{-1} corresponds to the asymmetric stretching vibration modes of the non-bridging oxygen (NBO) in the (Q^2) unit, and the band at 1170 cm^{-1} corresponds to the symmetric stretching vibration of (PO_2)⁻ in metaphosphate (Q^2) units.^[48] The intense band at 890 cm^{-1} is assigned to the short Nb—O bonding in isolated NbO_6 octahedra.^[46] The band at 820 cm^{-1} corresponds to the NbO_6 octahedra linked into chains,^[46,48] The band at 630 cm^{-1} is attributed to the Nb—O stretching mode of corner-shared NbO_6 octahedra and to the NbO_6 octahedra linked into a 3D network structure.^[46,48–51] The bands at 425 and 250 cm^{-1} correspond to O—Nb—O resonance bonding and Nb—O—Nb bonds in NbO_6 octahedra, respectively.^[48] The Raman spectrum of the Nb10 glass exhibits three additional bands at 740, 990, and 1040 cm^{-1} which correspond to stretching modes of P—O—P linkages, stretching of Q^0 (PO_4)³⁻, and vibration of Q^1 (PO_3)²⁻ groups in the polyphosphate chains, respectively.^[52,53] The increase in Nb_2O_5 concentration leads to an increase in the intensity of the bands at 250, 425, 630, and 820 cm^{-1} while the intensity of the bands at 740, 990, and 1040 cm^{-1} decreases.

The FTIR spectra (**Figure 2b**) show absorption bands centered around 530, 575, 630, 720, 850, 970, 1060, and 1130 cm^{-1} . The absorption band at 1130 cm^{-1} corresponds to the symmetric stretching vibration of PO_2 entities.^[54] The absorption band around 1060 cm^{-1} is assigned to the asymmetric and symmetric stretching vibration modes of non-bridging oxygen associated with Q^1 tetrahedra.^[54] The band near 970 cm^{-1} corresponds to Q^0 (PO_4)³⁻ groups.^[55] The bands near 850 and 720 cm^{-1} correspond to the asymmetric and symmetric stretching of pyrophosphate (Q^1) units, respectively.^[55] The band at around 630 cm^{-1} is attributed to Nb—O bonding from the NbO_6 octahedra.^[54] The absorbance band around 575 cm^{-1} is related to the coupled modes of O—Nb bonds and O—Nb—O—P, and the band around 530 cm^{-1} and vibration related to the bending of O—P—O bonds of (PO_4)³⁻ groups.^[56] The increase in Nb_2O_5 concentration leads to an increase in the intensity of the bands at 630, 575, and 530 cm^{-1} and a decrease in the intensity of the bands at 720, 850, 970, 1060, and 1130 cm^{-1} .

From the changes in the Raman and IR spectra, the addition of Nb_2O_5 leads to the formation of strong linkages such as

P—O—Nb and Nb—O—Nb at the expense of P—O—P bonds. The incorporation of Nb_2O_5 promotes the formation of NbO_6 octahedra linked to a 3D network at the expense of the 2D phosphate network. Such structural reinforcement of the vitreous network is confirmed by the observed increase in T_g with increasing Nb_2O_5 concentration. Additionally, the increase in Nb_2O_5 concentration leads to a redshift of the UV absorption edge (see **Figure 1b**). This shift of the optical band gap to longer wavelengths with increasing Nb_2O_5 content can be attributed to the increase in the refractive index and the difference in the ionic radii; since Nb^{5+} possesses a larger ionic radius than P^{5+} , its outer electron cloud interacts more strongly with the nearby non-bridging oxygens, facilitating electron-transfer at lower energy.^[55,57]

Composites were fabricated by adding 1 and 2.5 wt.% of $\text{YAG}:\text{Ce}^{3+}$ crystals in the Nb25 molten glass, selected due to its high refractive index. It is worth pointing out that the concentration of the crystals in the composites is below the sensitivity threshold of the diffractometer, and no corresponding peaks are observed in the XRD curves (**Figure S1b**, Supporting Information). The composite prepared with 1 wt.% of $\text{YAG}:\text{Ce}^{3+}$ crystals is translucent, whereas the other composite with a larger amount of crystals is opaque. The composites are more colored than in the as-prepared Nb25 glass, which might be a sign of the phosphor-glass reaction during the composite preparation. The transmittance significantly decreases by $\approx 70\%$, after embedding the $\text{YAG}:\text{Ce}^{3+}$ crystals in the glass matrix due to the mismatch of the refractive index between the $\text{YAG}:\text{Ce}^{3+}$ crystals and the glass, the large size of $\text{YAG}:\text{Ce}^{3+}$ crystals (expected to be up to 10 μm as per the supplier) and probably cluster of $\text{YAG}:\text{Ce}^{3+}$ crystals in the glass forming during the melting process (**Figure 3a**). **Figure 3b** shows the excitation spectra of the composites compared to those of the as-received crystals for an emission at 600 nm. The two excitation peaks at ≈ 345 and ≈ 460 nm correspond to the $4f^1$ (${}^2F_{7/2}$) \rightarrow $4f^05d^1$ (${}^2B_{1g}$) and $4f^1$ (${}^2F_{7/2}$) \rightarrow $4f^05d^1$ (${}^2A_{1g}$) electron transitions of Ce^{3+} ions, respectively.^[58,59] Noticeable mismatches are evident between the excitation bands of the composites and those of the as-received crystals. The reduction of the excitation band intensity at 345 nm is mostly attributed to the high absorption of the glass matrix in the UV region. The slight broadening of the band ≈ 460 nm when increasing $\text{YAG}:\text{Ce}^{3+}$ content is not fully understood; it might

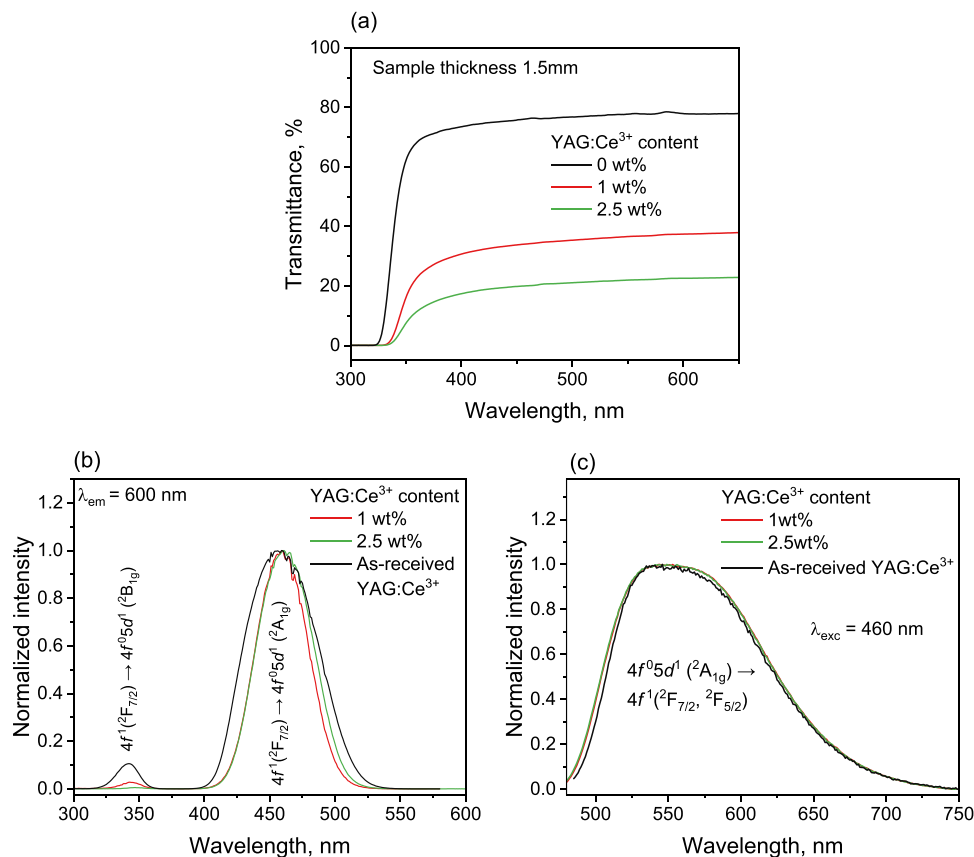


Figure 3. a) Transmittance spectra of the composites and undoped glass. b) Excitation spectra of the composites and as-received YAG:Ce³⁺ crystals collected at 600 nm. c) Emission spectra of the composites and as-received YAG:Ce³⁺ crystals under 460 nm excitation.

be associated with dipole-dipole interactions and energy migration arising from aggregation of YAG:Ce³⁺ phosphor particles at higher concentrations. At lower dopant densities, these interactions are reduced, resulting in a sharper excitation band.^[60,61] Figure 3c shows the normalized emission spectra of the composites and of the as-received crystals when 460 nm is used as excitation. The emission band covering the 500–700 nm range consists of an overlap of two emission bands centered at 580 and 520 nm, which are attributed to the $5d (^2A_{1g}) \rightarrow 4f (^2F_{7/2})$ and $5d (^2A_{1g}) \rightarrow 4f (^2F_{5/2})$ transitions of Ce³⁺ ions, respectively.^[58,59] No significant changes in the shape of the emission band were observed after embedding the phosphors in the glass, suggesting that the crystals survive the composite preparation process.

Although no significant changes are observed in the emission properties of the composites, notable differences emerge at the microscale. Figure 4a shows the micro-Raman spectra collected from the surface of the composite prepared with 1 wt.% of YAG:Ce³⁺. The micro-Raman and micro-luminescence spectra collected from the composite with 2.5 wt.% of YAG:Ce³⁺ can be found in Figure S2 (Supporting Information). The Raman spectra were collected from a crystal found at the surface of the composite, from the glass region of the composite, and at the crystal-glass interface. The Raman spectra were recorded in the 200–3000 cm⁻¹ range using a 785 nm laser excitation. It is known that for garnet crystals, there are no Raman-active modes above

900 cm⁻¹.^[62–64] The weak bands that appear in the wavenumber range (< 900 cm⁻¹) correspond to the internal modes related to AlO₄ groups.^[63,64] It is interesting to point out that the Raman spectrum of the crystal embedded in the glass is different from the Raman spectrum of the as-received crystals. After embedding the crystals in the glass, new peaks appear while others shift in position, suggesting changes in the structure of the YAG:Ce³⁺ crystals when embedded in the glass matrix. The Raman spectrum recorded from the glass region of the composite closely resembles that of the YAG:Ce³⁺ free glass, suggesting that the addition of YAG:Ce³⁺ phosphors in the glass does not have a significant impact on the structure of the glass matrix. The Raman spectrum at the interfacial crystal-glass region shows an overlap between the glass and crystal spectra. Figure 4b displays the micro-luminescence spectra of both the as-received and embedded YAG:Ce³⁺ crystals, revealing the typical emission band from Ce³⁺ ions that closely resembles the one observed in Figure 3c. Figure 4b also shows the intensity mapping of the emission at 580 nm under 532 nm laser excitation, confirming that crystals seen at the surface of the composite are YAG:Ce³⁺. No changes were observed in the shape of the emission band after embedding the YAG:Ce³⁺ crystals in the glass, except for the appearance of two emission peaks at around 700 nm, which could be attributed to Cr³⁺ impurities (Cr³⁺: $4T_{2g} \rightarrow 4A_{2g}$ and $2E_g, 2T_{1g} \rightarrow 4A_{2g}$).^[65] The Cr³⁺ is likely due to trace impurities present in the starting commercial YAG:Ce³⁺ powder, as is common for garnet hosts.

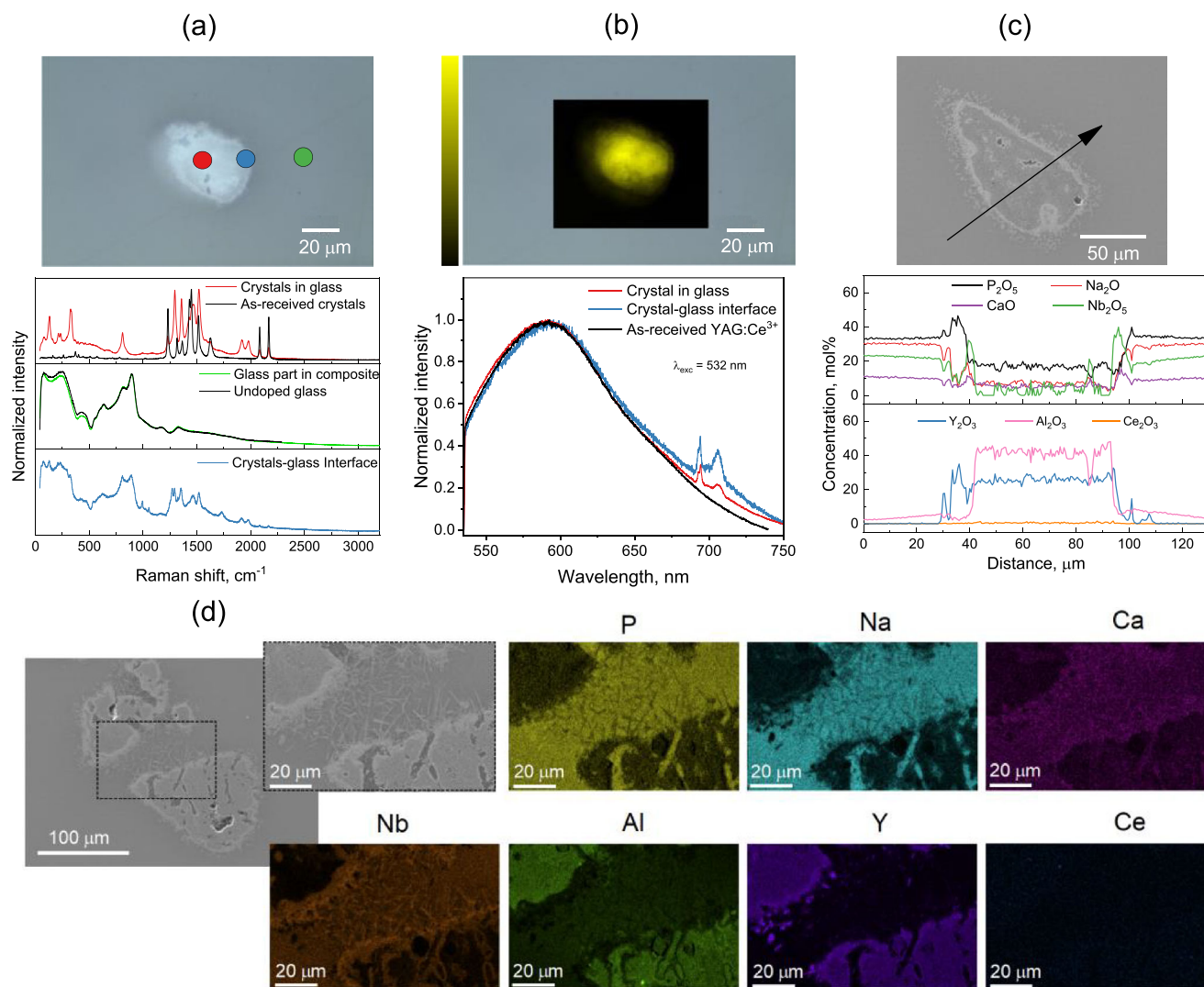


Figure 4. (a) Microscope image ($\times 50$) of a crystal found at the surface of the composite prepared with 1 wt.% of YAG:Ce^{3+} and micro-Raman spectra collected inside a crystal found at the composite surface, in the glass part of the composite, and at the crystal-glass interface. Also shown is the micro-Raman spectrum of a YAG:Ce^{3+} -free glass and of as-received YAG:Ce^{3+} crystals ($\lambda_{\text{exc}} = 785 \text{ nm}$). (b) Micro-luminescence mapping of intensity at 580 nm and micro-luminescence spectra inside the crystal found on the composite surface and the crystal-glass interface. Also shown is the micro-luminescence spectrum of the as-received YAG:Ce^{3+} crystals ($\lambda_{\text{exc}} = 532 \text{ nm}$). (c) SEM image and EDS line scan across a YAG:Ce^{3+} phosphor particle found at the surface of the composite. (d) Elemental mapping of the YAG:Ce^{3+} phosphor particle found at the surface of the composite.

Figure 4c shows an EDS line scan across the YAG:Ce^{3+} crystal located at the surface of the composite prepared with 1 wt.% of YAG:Ce^{3+} . The composition analysis suggests that the crystal retains its original composition in its center with an Al/Y ratio of ≈ 1.6 , which is in good agreement with the stoichiometry of YAG ($\text{Y}_3\text{Al}_5\text{O}_{12}$). However, at the YAG:Ce^{3+} crystal-glass interfacial region, this ratio deviates from the stoichiometric value. Additionally, Nb rich area is suspected at the YAG:Ce^{3+} crystal-glass interface, promoting crystallization as seen in the SEM image in Figure 4d, where needle-shaped features grow within the glass matrix near the boundary. It should be noted that the Ce mapping appears dark due to the low concentration of Ce^{3+} ions in the phosphors (2%, as per the supplier). The interfacial reaction between the glass and the embedded phosphors was reported in previous studies.^[31,66,67] Zhang et al suggested

that Na^+ and Ca^{2+} ions cause intrinsically severe corrosive reaction between the glass matrix and phosphors owing to the high reactivity and diffusivity of those low-valence ions.^[66] Nevertheless, the decomposition of YAG:Ce^{3+} phosphors during the melting process remains partial and localized, as the glass structure closely resembles that of the undoped glass, as previously discussed.

A crack-free composite preform (8 cm long and 1 cm in diameter) was successfully prepared with homogeneous dispersion of the YAG:Ce^{3+} crystals (1 wt.%) in the glass (Figure 5a). The translucent appearance of the preform suggests the absence of crystal agglomeration in the glass. Despite the presence of YAG:Ce^{3+} crystals, this composite preform was successfully drawn into a single-index fiber with a diameter of 400 μm . Figure 5b presents an SEM image of the fiber cross-section,

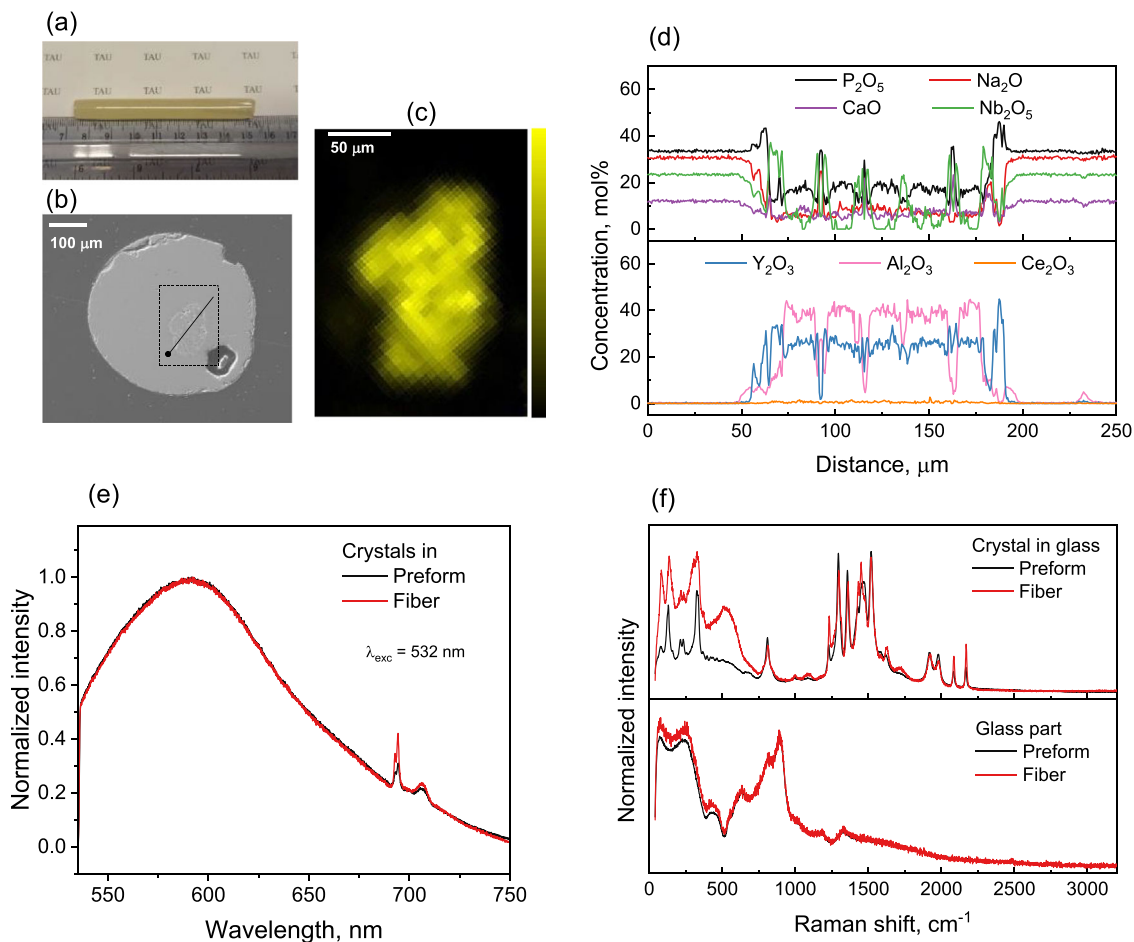


Figure 5. a) Picture of the composite preform prepared with 1 wt.% of the YAG:Ce³⁺ phosphors. b) SEM image of the fiber cross-section showing a YAG:Ce³⁺ crystal found at the cross-section surface, and c) micro-luminescence mapping of intensity at 580 nm of the crystal ($\lambda_{\text{exc}} = 532$ nm). d) EDS Line scan composition analysis across the crystal. e) Micro-luminescence spectra inside the crystal found in the preform and in the fiber ($\lambda_{\text{exc}} = 532$ nm). f) Micro-Raman spectra inside the crystal and glass parts of the fiber and preform ($\lambda_{\text{exc}} = 785$ nm).

showing a YAG:Ce³⁺ phosphor particle located at the surface, the presence of which was confirmed from the mapping of the intensity of the emission at 580 nm under 532 nm laser excitation (Figure 5c) and the composition analysis performed across the phosphors (Figure 5d). The EDS line scan (Figure 5d) shows that both the glass matrix and the crystal maintain their original compositions, with no significant elemental variations detected following fiber drawing, suggesting that the YAG:Ce³⁺ crystals survive the fiber fabrication process with no elongation or breakup. Figure 5e,f show the micro-luminescence and micro-Raman spectra collected from the crystal found in the preform and in the fiber, respectively. No significant changes in the shape of the (emission and Raman) bands are seen after fiber drawing, confirming that the drawing process has a limited impact on the YAG:Ce³⁺ phosphors. The fiber drawing process does not substantially alter the glass structure, although some structural modifications are expected due to the intense quenching that occurs during drawing stress, as discussed in Ref. [68,69]. The slight increase in intensity of the Raman band at ≈ 425 cm⁻¹ compared to the main band suggests an increased number of Nb—O bridging in NbO₆ octahedra during the drawing process. Similar subtle

molecular unit re-orientation during the new thermal history of the drawing process was reported during the drawing of tellurite glasses.^[6]

Despite being a single-index fiber, light confinement is still observed, and light propagation along the fiber is maintained for a distance up to 4 cm, as seen in Figure 6a. Both broadband lamp light and 455 nm LED light were successfully guided through the composite fiber. Light propagation over centimeter-scale arises from a combination of factors, including guiding via reflections at the glass-air boundary, high directionality of the input beam, which allows light to remain confined over short propagation lengths, as well as multiple scattering events and redirection of light along the fiber by the embedded particles and the surface defects. Figure 6b shows the transmitted output power from fibers with different lengths under broadband lamp excitation. As the fiber length increases, a clear reduction in output power is observed across the spectral range. The fiber attenuation loss is estimated to be between 3 and 5 dB cm⁻¹ at 600 nm, which is quite large compared to other phosphate glass optical fibers.^[70,71] The observed loss primarily originates from the scattering of the light on the phosphor particles

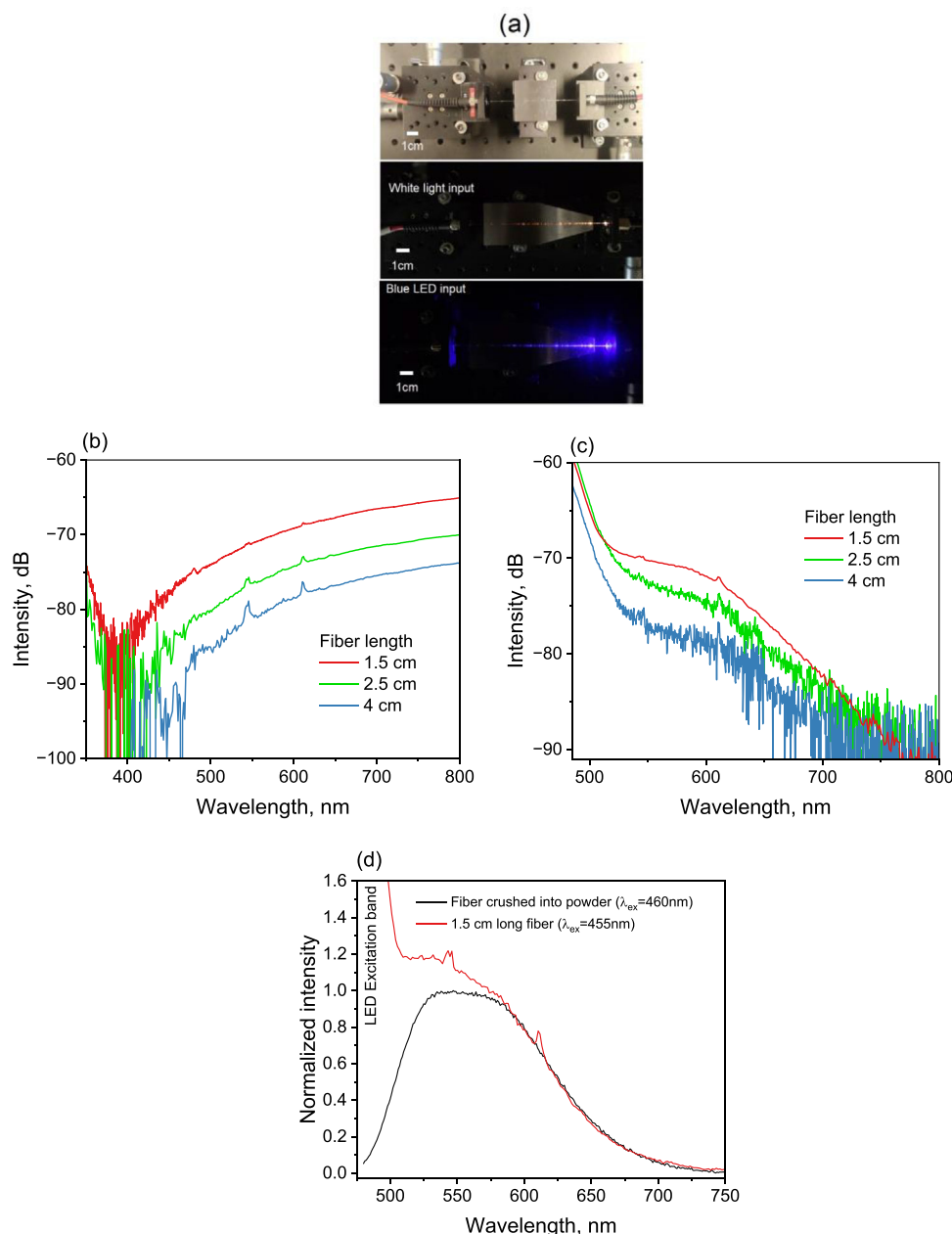


Figure 6. a) Pictures of the composite fibers containing 1 wt.% of YAG:Ce³⁺ phosphors. b) Transmission of fibers with different lengths under broadband lamp excitation. c) Emission of fibers with different lengths under 455 nm LED excitation. d) Normalized emission spectra measured from fiber crushed into powder ($\lambda_{exc} = 460$ nm) and collected at the output of a 1.5 cm long fiber under 455 nm LED excitation.

embedded within the fiber, surface defects, microcracks, and other imperfections, as well as the absence of the cladding and coating. Figure 6c shows the measured emission spectra from the fiber under 455 nm LED excitation. The high-intensity band observed below 525 nm corresponds to the unabsorbed broadband LED light passing through the fiber. The band covering the green-red region can be related to the emission from the Ce³⁺ ions (transitions: $5d^1 \rightarrow ({}^2F_{7/2}, {}^2F_{5/2})$).^[58,59] It is worth noting that increasing the length of the fiber does not lead to an increase in the overall intensity of the emission band in the green-red region. This observation indicates that attenuation remains predominant, sup-

pressing the gain associated with in-fiber white light generation. Consequently, the measured emission reflects the competing effects of optical attenuation and light generation within the fiber. Figure 6d compares the normalized emission spectra measured from a fiber crushed into powder ($\lambda_{exc} = 460$ nm) and at the output of the 1.5 cm long fiber under 455 nm LED excitation. Regardless of the overlap with the broadband LED excitation spectrum, using slightly different excitation wavelengths does not have a significant impact on the emission spectrum of YAG:Ce³⁺. Furthermore, comparison of the emission spectra confirms that the spectral shape of YAG:Ce³⁺ emission is preserved even after

propagation through the fiber. These results demonstrate both white light generation and light propagation in the newly developed composite fiber.

3. Conclusion

In this work, we have developed a new composite that can be drawn into a fiber. The composite was prepared by adding YAG:Ce³⁺ phosphors in the molten glass prior to quenching. To obtain a transparent composite, the glass composition was custom-engineered to achieve a refractive index match with the YAG:Ce³⁺ (1.83) by varying the Nb₂O₅ content in the NaPO₃-CaO-Nb₂O₅ glass. A single-index fiber was successfully drawn from a composite preform containing 1 wt.% of YAG:Ce³⁺ phosphor. It was found that the emission spectra of the composite bulks and fiber closely match in shape those of the as-receiving crystals, confirming that the YAG:Ce³⁺ phosphor particles survive both the fabrication and fiber drawing processes. However, the micro-Raman, SEM, and composition analyses reveal significant interactions between the YAG:Ce³⁺ phosphors and the surrounding glass matrix. Despite these interactions, the characteristic white light emission of the YAG:Ce³⁺ phosphors is preserved. The light propagation along the composite fiber is maintained for distances up to 4 cm. When a blue light from an LED is coupled into the fiber, the fiber exhibits visible emission in the range (500–750 nm) at the output. Despite limited emission efficiency from the fiber, this study serves as a proof of concept for integrating luminescent YAG:Ce³⁺ phosphors into optical fibers for white light generation.

4. Experimental Section

Preparation of the Glasses, Composites, and Fiber. Phosphate glasses with the composition of (75-x/2)NaPO₃ – (25-x/2)CaO – xNb₂O₅ (in mol%), where x = 10, 20, 25 mol% (referred to as Nb10, N20, and Nb25, respectively), were prepared by the conventional melting process. The raw materials of (NaPO₃)₆ (Thermo Fisher, 99.99%), CaCO₃ (Thermo Fisher, 99.99%), and Nb₂O₅ (Thermo Fisher, 99.99%) were weighed and well mixed with a mortar and pestle. The uniformly mixed stoichiometric compounds were melted in a platinum crucible at 1250 °C for 75 min in an air atmosphere with a 15 °C min⁻¹ heating rate. After melting, the glass melt was poured onto a brass plate and annealed in a muffle furnace at 40 °C below the glass transition temperature (*T_g*) for 8 h to release the residual mechanical stresses. It was challenging to obtain mechanically stable glasses with Nb₂O₅ concentrations higher than 25 mol%.

Composite bulks were prepared by adding 1 and 2.5 wt.% of the commercial YAG:Ce³⁺ crystals (Y_{2.94}Ce_{0.06}Al₅O₁₂, from Baikowski) into the molten glass with the composition 65.5NaPO₃ – 12.5CaO – 25Nb₂O₅ (in mol%) (Nb25). The mixture was manually stirred and poured onto a brass plate for rapid quenching to form the composite bulk. The composite preform was prepared by adding 1 wt.% of the YAG:Ce³⁺ crystals into the molten Nb25 glass, and then the liquid mixture was poured into a graphite mold preheated to 250 °C. The composites were then annealed at 40 °C below the glass *T_g* for 8 h.

The composite preform was polished and then drawn into a single-index fiber with a diameter of 400 μm as in Ref. [39]. The fiber was drawn at a temperature of 775 °C while a helium gas flow of 2.5 L min⁻¹ was used to ensure an inert environment. Polymer coating was not applied upon drawing to allow for investigation of the fiber pieces in powder form by external illumination. A schematic for the fabrication process is shown in Figure S3 (Supporting Information).

Characterization: The density of the glasses was obtained using Archimedes' method with ethanol as an immersion liquid. The results were obtained with an accuracy of ±0.02 g cm⁻³.

For refractive index measurement, the prism coupling technique with an Abbe refractometer (Model 2010/M, Metricon) was used at six different wavelengths: 443, 633, 825, 1061, 1312, and 1533 nm. The refractive index values were determined with an accuracy of ±0.001.

The transmittance spectra of the polished glasses and composites in the visible region were obtained using the UV–vis–NIR Spectrophotometer (UV-3600 Plus, Shimadzu), using samples of 1.5 mm thickness.

The FTIR spectra were measured using the FTIR2000 PerkinElmer spectrometer in attenuated total reflectance (ATR) model with a resolution of 2 cm⁻¹ and accumulation of 8 scans.

X-ray diffraction (XRD) patterns of the glasses and composites were obtained with a PANalytical EMPYREAN multipurpose X-ray diffractometer (PANalytical, Almelo, The Netherlands). The measurements utilized Ni-filtered Cu-Kα radiation, and the diffractograms were collected over a range of 2θ (10°–80°), with a measurement step of 0.05°.

The micro-Raman and micro-luminescence spectra were obtained using a confocal Raman microscope (Renishaw inVia Qontor, Wotton-under-Edge, UK) using 785 and 532 nm excitation lasers, respectively. The measurements were performed with a 50× objective lens and 1200 lines mm⁻¹ grating.

Emission spectra of the composite bulks and fiber were measured using an Edinburgh FLS1000 photoluminescence spectrometer equipped with a xenon lamp as an excitation source and a PMT-900 detector. Powder samples were used to perform the measurement. The emission spectra were recorded under excitation at 460 nm, whereas the excitation spectra were obtained at 600 nm. The emission and excitation spectra were obtained with 1 nm bandwidths.

A scanning electron microscope (SEM) (Crossbeam 540, Carl Zeiss, Oberkochen, Germany) equipped with an energy-dispersive spectroscopy (EDS) detector (X-MaxN 80, Oxford Instruments, Abingdon-on-Thames, UK) was used to obtain images and analyze the composition of the samples. To reduce charging effects, the samples were coated with a conductive carbon layer.

For the composite fiber characterization, two fiber-coupled excitation light sources were butt-coupled to the sample fiber. For white light generation, a fiber-coupled LED at 455 nm wavelength with 15 nm FWHM bandwidth (M455F3, ThorLabs, 400 μm multimode fiber) was used. For transmission measurements, a fiber-coupled halogen lamp white light source (Anritsu MG9224, 105 μm multimode fiber) was applied. The output light at the distal end was collected using a 200 μm multimode fiber and analyzed with an Optical Spectrum Analyzer (OSA, ANDO AQ6315B), within a spectral range of 350–800 nm.

The optical loss α (dB cm⁻¹) was estimated using the following equation:

$$\alpha = 10 \frac{\log\left(\frac{P_L}{P_I}\right)}{L - l} \quad (1)$$

where *P_L* and *P_I* are the transmitted output power of fibers with lengths *L* and *l*, respectively.

Supporting Information

Supporting Information is available from the Wiley Online Library or from the author.

Acknowledgements

This work was supported by the Research Council of Finland (Flagship Program, Photonics Research and Innovation PREIN-320165), Business Finland (OFFULA project-2689), and Jane and Aatos Erkkö Foundation (WhiFib- 31228013031).

Open access publishing facilitated by Tampereen yliopisto ja Tampereen ammattikorkeakoulu, as part of the Wiley - FinELib agreement.

Conflict of Interest

The authors declare no conflict of interest.

Data Availability Statement

The data that support the findings of this study are available from the corresponding author upon reasonable request.

Keywords

composite, phosphor in glass, white light source, YAG:Ce³⁺

Received: November 19, 2025

Revised: January 1, 2026

Published online: January 13, 2026

- [1] F. Abouraddy, M. Bayindir, G. Benoit, S. D. Hart, K. Kuriki, N. Orf, O. Shapira, F. Sorin, B. Temelkuran, Y. Fink, *Nat. Mater.* **2007**, *6*, 336.
- [2] Y. Tang, S. Anandasabapathy, R. Richards-Kortum, *Mol. Oncol.* **2020**, *15*, 2580.
- [3] Q. Shan, C. Wei, Y. Jiang, J. Song, Y. Zou, L. Xu, T. Fang, T. Wang, Y. Dong, J. Liu, B. Han, F. Zhang, J. Chen, Y. Wang, H. Zeng, *Light Sci. Appl.* **2020**, *9*, 163.
- [4] Z. Zhang, K. Guo, Y. Li, X. Li, G. Guan, H. Li, Y. Luo, F. Zhao, Q. Zhang, B. Wei, Q. Pei, H. Peng, *Nat. Photon.* **2015**, *9*, 233.
- [5] T. Sylvestre, E. Genier, A. N. Ghosh, P. Bowen, G. Genty, J. Troles, A. Mussot, A. C. Peacock, M. Klimczak, A. M. Heidt, J. C. Travers, O. Bang, J. M. Dudley, *J. Opt. Soc. Am. B* **2021**, *38*, F90.
- [6] A. L. Gaeta, *Femtosecond Optical Frequency Comb: Principle, Operation, and Applications* (Eds. J. Ye, S.T. Cundiff), Springer, Boston, MA, USA, **2005**.
- [7] Y. Pang, X. Lu, X. Zhang, Z. Miao, M. Sun, G. Tang, J. Li, Q. Zhao, C. Yang, D. Chen, Q. Qian, Z. Xu, *Materials* **2024**, *17*, 3426.
- [8] H. Wang, J. Zou, C. Dong, T. Du, B. Xu, H. Xu, Z. Cai, Z. Luo, *Opt. Lett.* **2019**, *44*, 4423.
- [9] J. Markiewicz, M. Kochanowicz, T. Ragiń, P. Miluski, W. A. Pisarski, J. Pisarska, M. Kuwik, D. Dorosz, M. Leich, M. Jäger, *Sci. Rep.* **2025**, *15*, 4161.
- [10] X. Wang, H. Ming, W. Huang, *Passive Components and Fiber-Based Devices II* **2005**, 6019, 931.
- [11] Y. Shi, M. Zhang, K. Chen, W. Deng, X. Liu, H. Su, J. Xie, X. Wang, J. Wan, H. Wang, *J. Non-Cryst. Solids* **2023**, *606*, 122200.
- [12] F. Ren, C. Song, Y. Cong, Y. Wu, Y. Bai, D. Zhou, *Ceram. Int.* **2023**, *49*, 32850.
- [13] P. Vařák, M. Kamrádek, J. Mrázek, O. Podrazký, J. Aubrecht, P. Peterka, P. Nekvindová, I. Kašík, *Opt. Mater. X* **2022**, *15*, 100177.
- [14] I. V. Zhlyukova, V. A. Kamynin, D. A. Korobko, A. S. Abramov, A. A. Fotiadi, A. A. Sysoliatin, V. B. Tsvetkov, *Photonics* **2022**, *9*, 773.
- [15] C. A. Whittaker, A. Perret, C. W. Fortier, O.-M. Tardif, S. A. Lamarre, S. Morency, D. Larivière, L. Beaulieu, Y. Messaddeq, C. N. Allen, *ACS Appl. Nano Mater.* **2020**, *3*, 6478.
- [16] P. K. Das, N. Dhiman, S. Umapathy, F. Gérôme, A. Bhardwaj, *Adv. Photonics Res.* **2023**, *4*, 2300167.
- [17] G. Liang, Y. Tang, J. Huang, J. Li, Y. Yuan, S. Yang, Z. Li, *Nanomaterials* **2021**, *11*, 2100.
- [18] M. Giroux, Z. Zahra, O. A. Salawu, R. M. Burgess, K. T. Ho, A. S. Adeleye, *Environ. Sci.: Nano.* **2022**, *9*, 867.
- [19] A. Shakhno, T. Zorenko, S. Witkiewicz-Lukaszek, M. Cieszko, Z. Szczepański, O. Vovk, S. Nizhankovskiy, Y. Siryk, Y. Zorenko, *Materials* **2023**, *16*, 2701.
- [20] K. Li, C. Shen, presented at *5th Int. Symp. on Advanced Optical Manufacturing and Testing Technologies: Optoelectronic Materials and Devices for Detector, Imager, Display, and Energy Conversion Technology*, Dalian, China, April **2010**.
- [21] F. A. Selim, A. Khamsehchi, D. Winarski, S. Agarwal, *Optic. Mater. Expr.* **2016**, *6*, 3704.
- [22] J. Dwivedi, P. Kumar, A. Kumar, Sudama, V. N. Singh, B. P. Singh, S. K. Dhawan, V. Shanker, B. K. Gupta, *RSC Adv.* **2014**, *4*, 54936.
- [23] R. Zhang, H. Lin, Y. Yu, D. Chen, J. Xu, Y. Wang, *Laser Photonics Rev.* **2014**, *8*, 158.
- [24] Y. Xu, Y. Li, R. Lei, Y. Hua, F. Huang, S. Xu, *J. Lumin.* **2023**, *263*, 120110.
- [25] S. N. Qadri, W. Kim, S. Bayya, L. B. Shaw, S. B. Qadri, J. Kolis, B. Stadelman, J. Sanghera, *Coatings* **2021**, *11*, 644.
- [26] S. Bao, Y. Liang, L. Wang, L. Wang, L. Xu, Y. Wang, X. Liang, W. Xiang, *ACS Sustainable Chem. Eng.* **2022**, *10*, 8105.
- [27] H. C. Yoon, K. Yoshihiro, H. Yoo, S. W. Lee, J. H. Oh, Y. R. Do, *Sci. Rep.* **2008**, *8*, 7412.
- [28] M. Y. Mehr, A. Bahrami, W. D. van Driel, X. J. Fan, J. L. Davis, G. Q. Zhang, *Int. Mater. Rev.* **2019**, *65*, 102.
- [29] H. Segawa, S. Ogata, N. Hirotsaki, S. Inoue, T. Shimizu, M. Tansho, S. Ohki, K. Deguchi, *Opt. Mater.* **2010**, *33*, 170.
- [30] Y. K. Lee, J. S. Lee, J. Heo, W. B. Im, W. J. Chung, *Opt. Lett.* **2012**, *37*, 3276.
- [31] X. Xiang, B. Wang, H. Lin, J. Xu, J. Wang, T. Hu, Y. Wang, *J. Eur. Ceram. Soc.* **2018**, *38*, 1990.
- [32] S. Kudo, A. Kishioka, H. Kuwahara, H. Kuroe, H. T. Hintzen, K. Itatani, *J. Am. Ceram. Soc.* **2019**, *102*, 1259.
- [33] E. S. Magalhães, A. Sedda, B. Bondzior, S. Vuori, D. Van der Heggen, P. F. Smet, M. Lastusaari, L. Petit, *Ceram. Int.* **2023**, *49*, 41150.
- [34] N. Vakula, M. Bardins, K. Nasser, B. Bondzior, C. Boussard-Plédel, J. Troles, L. Petit, *ACS Omega* **2025**, *10*, 16430.
- [35] J. Zhao, X. Zheng, E. P. Schartner, P. Ionescu, R. Zhang, T.-L. Nguyen, D. Jin, H. Ebendorff-Heidepriem, *Adv. Opt. Mater.* **2016**, *4*, 1507.
- [36] M. Yamashita, T. Imamura, S. Matsumoto, M. Murakami, T. Hongo, T. Akai, Y. Iwamoto, *KEM* **2016**, *702*, 113.
- [37] S. Tao, Y. Ping, F. Huang, Y. Hua, P. Qiao, Z. Xu, Y. Li, H. Ma, *Ceram. Int.* **2023**, *49*, 19606.
- [38] C. F. Bohren, D. R. Huffman, *Absorption and Scattering of Light by Small Particles*, John Wiley & Sons, New York, USA **2008**.
- [39] A. Lemiere, A. Szczodra, S. Vuori, B. Bondzior, T. W. Hawkins, J. Ballato, M. Lastusaari, J. Massera, L. Petit, *Mater. Res. Bull.* **2022**, *153*, 111899.
- [40] J. Lee, Y. Wei, P. Ren, J. Akhtar, Y. Lu, H. Ebendorff-Heidepriem, S. Jackson, *Adv. Optic. Mater.* **2024**, *12*, 2401536.
- [41] A. A. Stolov, D. A. Simoff, J. Li, *J. Light Technol.* **2008**, *26*, 3443.
- [42] S. Cui, J. Massera, M. Lastusaari, L. Hupa, L. Petit, *J. Non-Cryst. Solids* **2016**, *445–446*, 40.
- [43] D. E. Zelmon, D. L. Small, R. Page, *Appl. Opt.* **1998**, *37*, 4933.
- [44] L. Koudelka, P. Kalenda, P. Mošner, L. Montagne, B. Ravel, *J. Non-Cryst. Solids* **2021**, *572*, 121091.
- [45] S. L. Meena, P. Deedwaniya, *Appl. Phys. A* **2023**, *129*, 792.
- [46] A. Flambard, J. J. Videau, L. Delevoye, T. Cardinal, C. Labrugère, C. A. Rivero, M. Couzi, L. Montagne, *J. Non-Cryst. Solids* **2008**, *354*, 3540.
- [47] R. D. Shannon, *Acta. Cryst.* **1976**, *32*, 751.
- [48] A. Senapati, S. K. Barik, R. V. Krishnan, S. Chakraborty, H. Jena, *J. Therm. Anal. Calorim.* **2023**, *148*, 355.
- [49] S. Benyounoussy, L. Bih, F. Muñoz, F. Rubio-Marcos, *Heliyon* **2021**, *7*, 07113.
- [50] K. Griebenow, C. B. Bragatto, E. I. Kamitsos, L. Wondraczek, *J. Non-Cryst. Solids* **2018**, *481*, 447.
- [51] L. Bih, M. Azrou, B. Manoun, M. P. F. Graça, M. A. Valente, *J. Spectrosc.* **2013**, *2013*, 1.
- [52] H. Maeda, S. Lee, T. Miyajima, A. Obata, K. Ueda, T. Narushima, T. Kasuga, *J. Non-Cryst. Solids* **2016**, *432*, 60.

- [53] Y. Attafi, S. Liu, *J. Non-Cryst. Solids* **2016**, 447, 74.
- [54] Y.-M. Lee, S. M. Hsu, S. W. Yung, T. Zhang, Y. S. Huang, J. J. Wu, C. H. Hsu, T. S. Chin, *Mater. Chem. Phys.* **2014**, 144, 235.
- [55] C. M. Chu, J. J. Wu, S. W. Yung, T. S. Chin, T. Zhang, F. B. Wu, *J. Non-Cryst. Solids* **2011**, 357, 939.
- [56] F. F. Sene, J. R. Martinelli, L. Gomes, *J. Non-Cryst. Solids* **2004**, 348, 30.
- [57] J. A. Duffy, *Phys. Chem. Glasses* **2001**, 42, 151.
- [58] W. Zhao, S. Anghel, C. Mancini, D. Amans, G. Boulon, T. Epicier, Y. Shi, X. Q. Feng, Y. B. Pan, V. Chani, A. Yoshikawa, *Opt. Mater.* **2011**, 33, 684.
- [59] R. R. Jacobs, W. F. Krupke, M. J. Weber, *Appl. Phys. Lett.* **1978**, 33, 410.
- [60] M. Borlaf, M. Frankowska, W. W. Kubiak, T. Graule, *Mater. Res. Bull.* **2018**, 100, 413.
- [61] Y.-C. Lin, M. Bettinelli, S. K. Sharma, B. Redlich, A. Speghini, M. Karlsson, *J. Mater. Chem. C* **2020**, 8, 14015.
- [62] W. Dewo, V. Gorbenko, Y. Zorenko, T. Runka, *Opt. Mater. X* **2019**, 3, 100029.
- [63] K. Papagelis, G. Kanellis, S. Ves, G. A. Kourouklis, *phys. stat. sol. b* **2002**, 233, 134.
- [64] S. Kostić, Z. Ž. Lazarević, V. Radojević, A. Milutinović, M. Romčević, N. Ž. Romčević, A. Valčić, *Mater. Res. Bull.* **2015**, 63, 80.
- [65] T. Li, W. Wang, Q. Liu, Y. Wang, Z. Zhou, C. Hu, J. Li, *J. Inorg. Mater.* **2025**, 40, 1037.
- [66] D. Zhang, W. Xiao, C. Liu, X. Liu, J. Ren, B. Xu, J. Qiu, *Nat. Commun.* **2020**, 11, 2805.
- [67] H. Lin, T. Hu, Y. Cheng, M. Chen, Y. Wang, *Laser Photonics Rev.* **2018**, 12, 1700344.
- [68] J. Massera, A. Haldeman, D. Milanese, H. Gebavi, M. Ferraris, P. Foy, W. Hawkins, J. Ballato, R. Stolen, L. Petit, K. Richardson, *Opt. Mater.* **2010**, 32, 582.
- [69] R. Gumenyuk, A. Poudel, T. Jouan, C. Boussard-Plédel, T. Niemi, L. Petit, *Opt. Mater. Express* **2017**, 7, 4358.
- [70] P. Lopez-Iscoa, N. Ojha, D. Pugliese, A. Mishra, R. Gumenyuk, N. G. Boetti, D. Janner, J. Troles, B. Bureau, C. Boussard-Plédel, J. Massera, D. Milanese, L. Petit, *J. Am. Ceram. Soc.* **2019**, 102, 6882.
- [71] E. Ceci-Ginistrelli, D. Pugliese, N. G. Boetti, G. Novajra, A. Ambrosone, J. Lousteau, C. Vitale-Brovarone, S. Abrate, D. Milanese, *Opt. Mater. Express* **2016**, 6, 2040.